The *BABAR* Detector

Official *BABAR* author list goes here

The BABAR detector has been designed for optimal studies of CP violation in B decays produced by asymmetric-energy e^+e^- collisions at PEP II.

7. Electromagnetic Calorimeter

FOR INTERNAL DISTRIBUTION ONLY
Version 9
Nov 2000

7.1. Design Requirements

The *BABAR* electromagnetic calorimeter is required to detect low energy photons with high efficiency, and to precisely measure their energy and direction. It is also the primary sub-detector providing electron - hadron separation. The efficient reconstruction of extremely rare decays of B mesons containing π^0 s (e.g. $B^0 \to \pi^0\pi^0$) pose the most stringent design requirements on energy resolution of order 1% while excellent photon efficiency at low energies ($\mathcal{O}$ (20 MeV)) is required for efficient reconstruction of B meson decays containing multiple π^0 and η [1]. Similar precision is required for efficient separation of electrons and hadrons with purities required at the 0.1% level for momentum as low as 500 MeV/c. The need for high efficiency requires hermetic coverage of the acceptance region while excellent resolution can only be achieved by minimizing the material in front and between the active detector elements. In addition we require high efficiency in data taking over the lifetime of the experiment. This implies that all inaccessible detector elements must be highly reliable and that routine detector maintenance such as calibrations be performed with minimal interference to normal detector operation.

7.2. Implementation

CsI(Tl) scintillator is a natural technology choice to achieve our design requirements. The electromagnetic calorimeter is a hermetic - total absorption array of 0.1% thallium iodide doped cesium iodide (CsI(Tl))crystals, read out with solid state photo-detectors matched to the spectrum of scintillation light. Crystals are arranged quasi-projectively in a barrel-endcap geometry (Figure 1). The high light yield and small Moliere radius gives the excellent energy and position resolution required, while the short radiation length guarantees complete shower containment at *BABAR* energies with a relatively compact design. Furthermore, the high light yield and peak of the emission spectrum permit efficient use of a silicon photodiode readout. This readout chain is itself compact and most importantly allows the calorimeter to be located within the magnetic solenoid volume, minimizing the material in front of the detector which can cause pre-showering. The transverse size of the crystals is chosen to be comparable to the Moliere radius achieving the required angular resolution at low energies of a few milliradians. This modest Moliere radius also limits the total number of crystals (and readout channels) to an acceptable level.

Table 1
Properties of CsI(Tl) .

Radiation Length	1.85 cm
Moliere Radius	3.6 cm
Density	4.53 g/cm^3
Light Yield	50000 γ/ MeV
Light Yield Temp. Coeff.	0.1 %/°C
Peak Emission λ_{max}	565 nm
Refractive Index (λ_{max})	1.79
Decay Time	680 ns (64%)
	3.34 μs (36%)

The energy resolution of a calorimeter is determined by fluctuations in the electromagnetic shower propagation and in the case of a homogeneous crystal detector is empirically described by equation 1. The resolution as a function of energy E is given by σ_E parameterized as the quadratic sum of a stochastic term σ_1 and a constant term σ_2.

$$\frac{\sigma_E}{E} = \frac{\sigma_1}{\sqrt[4]{E}} \oplus \sigma_2 \quad (1)$$

The stochastic term which is dominant at at low energies (< 100 MeV) arises from fluctuations in photon statistics and electronic noise in the readout chain. If care is taken to minimize the light loss fluctuations from showers traversing non-sensitive gaps and inter-crystal material while maximizing the light transmission into the photodiodes, this term can be reduced to 1-2% in CsI(Tl), where we have assumed that the coherent and incoherent noise introduced by the readout system can be reduced to have negligible impact on the resolution. This demands the design of low noise electronics and also the implementation of a real-time digital signal processing algorithm to achieve optimal performance (section 7.4).

The constant term, dominant at higher energies (> 1 GeV), arises from several effects. Firstly fluctuations in shower containment due to leakage out the rear of the crystal, albedo, absorption of energy in the inter-crystal support materials and from pre-showering in the materials in front of the crystal. These effects can be minimized by appropriate choice of the detector geometry and support structure material; their impact on resolution is constant in time. Secondly the light yield can vary along the length of the crystal due to variations in doping during growth, and variations in the reflective properties of the crystal surface and wrapping. Finally, changes in the scintillation and light transmission properties of CsI(Tl) due to radiation damage during normal operation, can also contribute to the constant term.

Non-uniformities result in a non-linear energy response as mean shower depth varies logarithmically with incident energy. Some can be reduced to negligible levels at the onset, by careful quality assurance of the crystals and wrapping procedures during construction. However, radiation damage during operation causes a degradation in response that changes with time. This requires a novel energy dependent calibration and monitoring system which employs a radioactive source, a light pulser, and reconstructed data. These calibrations must be updated every few days during operation, and be fully automated to track time dependent radiation damage effects. Residual uncertainties in this calibration combined with shower fluctuations contributes to a degradation in resolution.

The inaccessibility of crystals following assembly and the requirement of a ten year lifetime with no single crystal failures has been addressed by a combination of extensive accelerated aging tests during the design phase, and dual redundancy in the readout chain. Procedures developed during the design phase were imposed during assembly by strict quality control.

7.3. Mechanical Design/Physical Description

Table 2
CsI(Tl) Crystal Geometry. The detector is arranged in 56 axially symmetric rings (Figure 1).

$\cos\theta$ Interval	Length (X_0)	# Rings	Crystals /Ring
Endcap			
$0.956 - 0.962$	16.5	1	80
$0.948 - 0.955$	17.6	1	80
$0.923 - 0.947$	17.6	3	100
$0.892 - 0.922$	17.6	3	120
Barrel			
$0.794 - 0.890$	17.6	7	120
$0.621 - 0.793$	17.1	7	120
$0.350 - 0.620$	16.6	7	120
$-0.774 - 0.349$	16.1	27	120

The calorimeter is constructed in a cylindrical barrel-endcap geometry and extends over the full 2π range azimuthally to give 90% solid-angle cov-

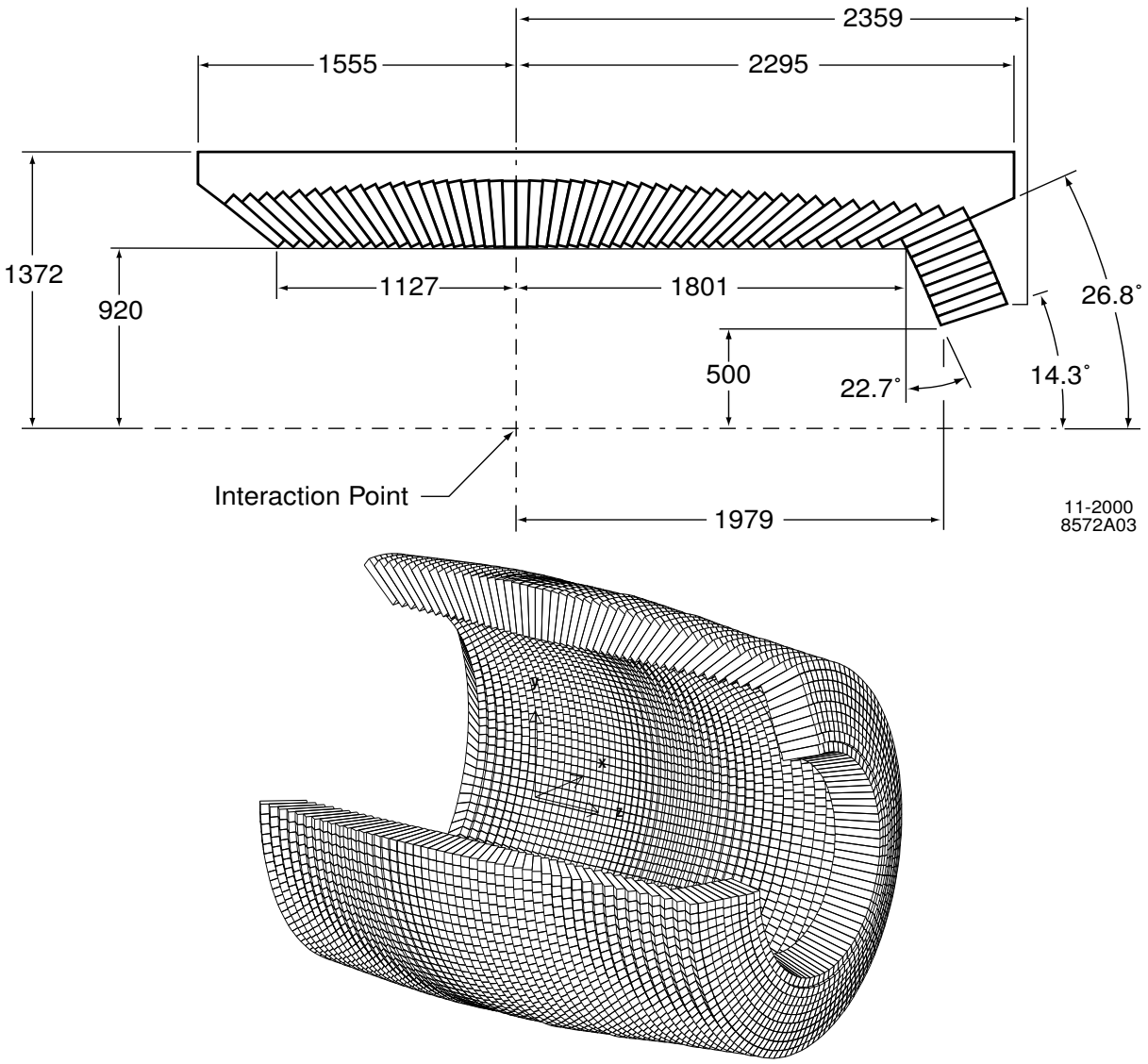

Figure 1. The crystal geometry of the Electromagnetic Calorimeter. A cross-sectional view in the vertical-beam axis plane is shown. The detector is symmetric about the beam axis. All dimensions are in mm.

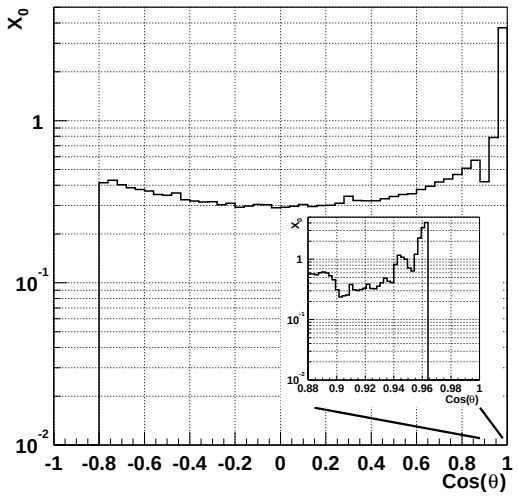

Figure 2. The material (X_0) in front of the calorimeter at different polar angles, $\cos\theta^{\cdot}$

erage (Figure 1 and Table 2). The barrel contains 5760 crystals divided into 48 distinct rings along its length; each ring contains 120 crystals. The endcap extends from the barrel with an additional 820 crystals divided into 8 rings for a total of 6580 crystals. The crystals have a tapered trapezoidal cross-section and increase in length from the backward to the forward direction to offset the effects of shower leakage from the increasing average particle energy. To minimize the probability of pre-showering, the crystals are supported at the outer radius, with only a thin gas seal at the front. The barrel and adjoining first four rings of the endcap have less than $0.6X_o$ (Figure 2) of material directly in front while the SVT support structure shadows the inner four rings of the endcap with 0.6-3.0 X_o being worst for the innermost ring.

To reduce the impact of inter-crystal material, the crystals are aligned projectively with respect to the beam interaction point (IR) in the azimuthal direction but are offset in the polar direction to be non-projective. This offset is graded to increase from 14 milliradians in the back barrel to 38 milliradians as the 8mm barrel-endcap gap is approached, and then diminish to 14 milliradians in the endcap.

The crystals were grown in boules from a melt of raw CsI salt doped with Thallium [2]. The crystals were cut from the boules and then machined into tapered trapezoids. Each of the 56 rings contains a differently dimensioned crystal to achieve the hermetic coverage. Each crystal is machined to a tolerance of ± 150 μm . The crystal surfaces are then polished. The tapered crystals act not only as a total absorption scintillating medium but also as a guide to direct light to the rear mounted photodiodes. At the polished crystal surface light is both internally reflected and lost by transmission. The lost light is recovered in part by wrapping the crystal in two layers of diffuse white reflector, 165 μm TYVEK ^{TM}. A diffuse reflector is empirically favored over a specular reflector. The uniformity of light yield along the wrapped crystal is measured during quality assurance by scanning a highly collimated radioactive source at 20 points along its length. It is adjusted to be within $\pm 2\%$ in the front half of the crystal increasing to $\pm 5\%$ in the rear face by selectively degrading the crystal surface to reduce its reflectivity. The crystal is further wrapped in 25 μm of aluminum foil which is electrically connected to the photodiode and preamplifier housing to provide a Faraday shield. The aluminum is then wrapped in 13 μm Mylar to electrically isolate it from the mechanical support structure.

The photon detector consists of two $2 \times 1\,\mathrm{cm}^2$ silicon PIN diodes (Hamamatsu S-2744-08) mounted on a transparent 1mm thick polyethylene plate of the same area. The remaining area of the crystal face is covered by a plastic plate with white reflective paint. There are two 3 mm holes to access the fibers which transmit light from the light pulser monitoring system. The diodes are epoxied to the plate and the plates to the crystal using an optical epoxy to maximize light transmission. The diodes are directly connected to a pair of low noise preamplifiers and the entire assembly housed in an aluminum and brass fixture as shown in Figure 3. This fixture is electrically

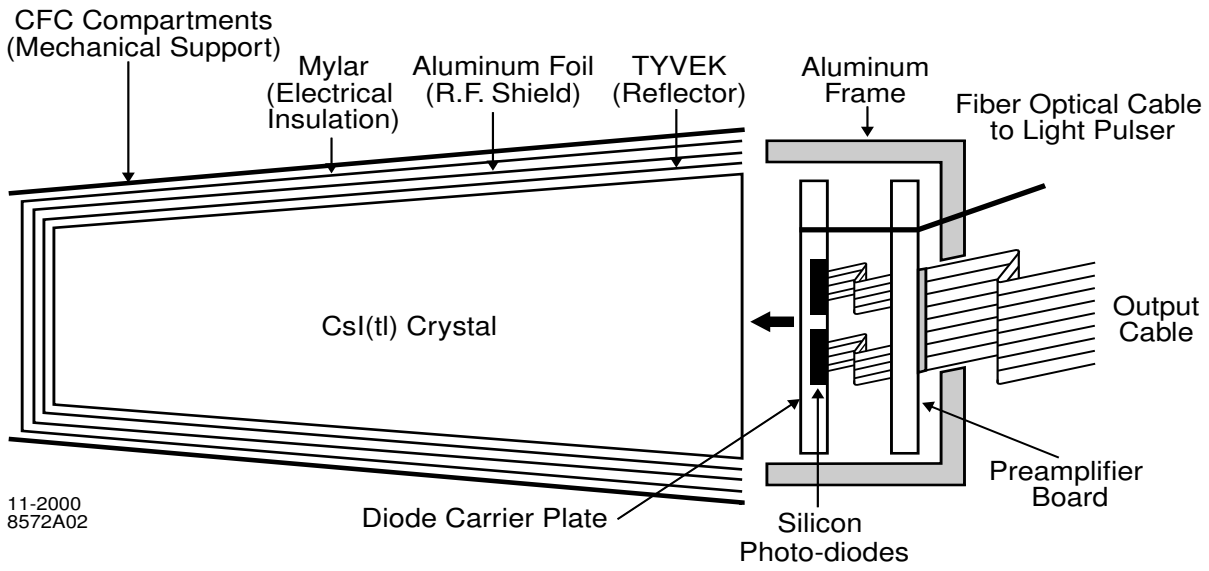

Figure 3. The assembly of the front-end readout package mounted on the rear face of the crystal.

coupled to the aluminum foil wrap of the crystal using a silver conductive epoxy and thermally coupled to the support frame, which itself is locally cooled to dissipate the 100 mW load from the two preamplifiers.

The mechanical support of the wrapped and instrumented crystals minimizes inter-crystal materials while exerting minimal force on the crystal surfaces; this prevents deformations and surface degradation that could compromise performance. Support is achieved by an "eggcrate" structure of thin walled (300 μm) carbon fiber epoxy composite (CFC)(Figure 4). Each compartment holds a single crystal package loosely in its pocket to guarantee that the forces on the crystal surfaces never exceed its own weight.

The structure is fabricated in 280 separate modules of 7×3 crystals. After crystal and photodiode insertion the aluminum readout assembly which also acts to stiffen the module, is attached with thermally-conducting epoxy into the CFC module. The entire module is then bolted and again thermally epoxied to an aluminum strong back, which allows handling of the 100 kg package in all orientations. The strong back contains alignment features as well as channels to couple into the cooling system. Each module is subsequently aligned and its strong back bolted to a 1 inch thick cylindrical aluminum support cylinder that runs the length of the detector. On its thick annular end-flanges this cylinder contains alignment dowels and mounting features for the forward endcap and access ports for digitizing electronics crates. The end-flanges also contain channels for cooling of the digitization electronics.

The endcap itself is similarly constructed of 20 CFC modules (each with 41 crystals) individually aligned and bolted to two semicircular "C" support elements so that the endcap calorimeter can be retracted and separated into two halves to facilitate access to the central detector components. The endcap modules can be dismounted and repaired, should radiation damage become a problem.

The barrel support cylinder carries the load of all barrel modules plus the forward endcap to

the magnet iron through four flexible supports. These decouple and dampen any acceleration of the calorimeter induced by the movement of the magnet iron during an earthquake.

The entire calorimeter is surrounded by a double Faraday shield composed of two 1 mm aluminum plates so that the diodes and preamplifiers are further isolated from external noise. This cage also serves as the environmental barrier, allowing the slightly hygroscopic crystals to reside in a dry nitrogen atmosphere.

It is important that the crystals and readout be maintained at this constant accurately monitored temperature so that the crystal epoxy joints are not mechanically stressed by the different thermal expansion coefficients of the CsI(Tl) and the diode carrier plate. A complete fracture of this joint would lead to a 25 % loss in signal. Heat sources include the preamplifiers(100 mW/crystal) and the digitizing electronics (6 kW). Preamplifier heat is removed by conduction through a thermal path to the module strong backs which are directly cooled by an active fluorinert ^{TM} system. The digitizing electronics are housed in 80 mini-crates, each in contact with the annular end-flanges. These are indirectly cooled by chilled water pumped through channels milled into the inner and outer radii of the end-flanges.

Aging tests of the diode-crystal joint included repeated daily thermal cycling to $\pm 5^{o}C$ and revealed no significant deteroration. This allowed us to set a conservative requirement for operation at 20 $\pm 0.5°C$. During construction, temperature was strictly maintained by central control of the assembly and test areas. The entire detector is interlocked so that it is not possible to have a rapid change in temperature of more than $\pm 3°C$. In one year of operation we have observed no failures of these epoxy joints.

7.4. Electronics

7.4.1. Electronics Design Requirements and Implementation.

The electronic readout system, shown schematically in Figure 5, is required to have negligible impact on the energy resolution for electromagnetic showers in the range few MeV - 13 GeV. The lower bound accommodates the use of a 6 MeV radioactive source for calibration; in data taking a practical lower bound is 20 MeV. This leads to a requirement of less than 250 keV equivalent noise energy (ENE) and to a digitization scheme with an effective 18 bit dynamic range in which the least significant bit at the lowest energies is 50 keV. At high energies, minimizing the noise contribution to the constant term of equation **??** requires the coherent component be significantly smaller than the incoherent one. In addition we require that the resolution not be degraded significantly by the presence of high rates of low energy (<5 MeV) beam-related photon backgrounds. Finally the inaccessibility of the crystals leads to a reliability requirement on the front-end components that we be able to readout all crystals for 10 years without repair.

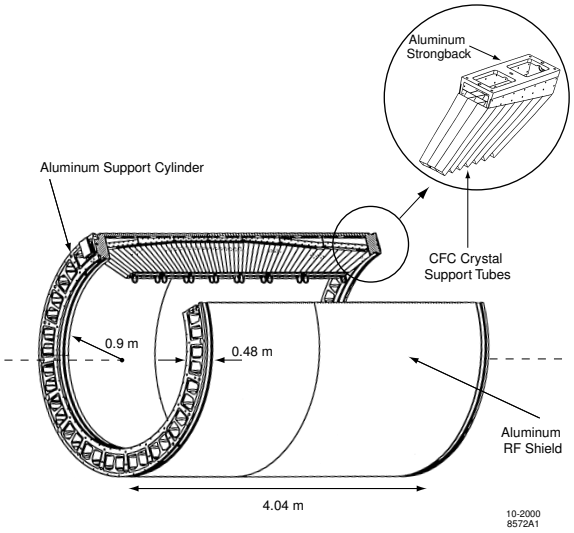

Figure 4. The support structure and assembly of the barrel.

The ENE is the ratio of the electronic noise charge of the readout system to the signal charge produced by the photon detector for an electromagnetic shower. Minimizing the ENE requires a high scintillation light yield into the photon detector, a highly efficient photon detector and a low

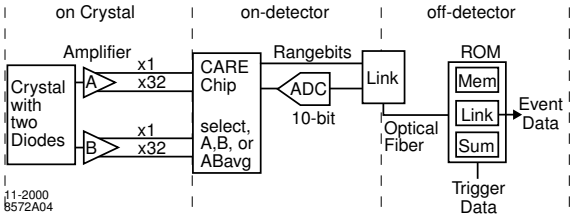

Figure 5. A schematic diagram of the readout electronics for the Electromagnetic Calorimeter.

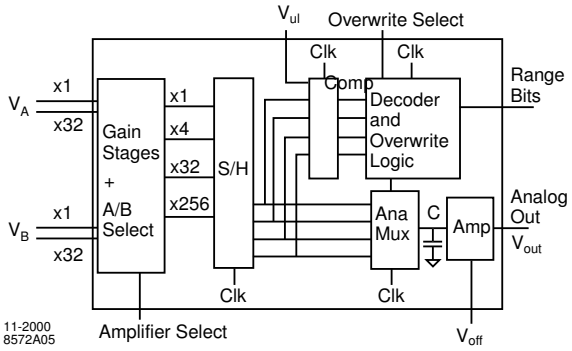

Figure 6. The Custom Auto-Range Encoding (CARE) chip.

noise readout scheme. Low noise (low leakage current) silicon PIN photo-diodes [10] are used as the photon detector. The photo-diodes have a quantum efficiency of 70% for the CsI(Tl) scintillation light. The electronic noise is due to the intrinsic thermal and shot noise of these devices. It is proportional both to the dark current and to the capacitance into the readout preamplifier. The preamplifier is a low-noise charge sensitive amplifier implemented as a fully custom ASIC [11]. It shapes the signal into a pulse with a characteristic shaping time and acts as a band-pass filter to remove high and low frequency noise components not-associated with the signal. The optimal shaping time for CsI(Tl), corresponding to the lowest noise, would be 2-3 μs but a shorter shaping time is chosen in order to reduce the probability of overlap with low energy photons from beam backgrounds. The shaping is implemented in a three stage filter CR-RC-RC with shaping times of $0.8\,\mu s - 0.25\,\mu s - 0.25\,\mu s$. The commensurate degradation in noise performance is recovered later in the readout chain by implementing a real-time digital signal processing algorithm following digitization. The input capacitance to the preamplifier is minimized by mounting the preamplifer directly upon the photo-diodes, eliminating the extra capacitance of a connecting cable. The preamplifier is connected to the post-amplification/digitization stage by a shielded ribbon cable that runs the length of the support cylinder, to the mini-crates in the end-flanges.

A study of the failure rates of the inaccessible front-end readout components leads to a dual redundancy in both photo-diodes and preamplifiers in order to achieve our reliability requirement. The dual signals are combined in the post-amplification/digitization stage, at a point accessible for maintenance.

It is technically very difficult and expensive to build an entire readout chain as an 18 bit dynamic range system. In particular the susceptibility of cables to noise makes it inadvisable to transmit more than 13 bit signals between the readout components. A range encoding scheme implemented by the Custom Auto-Range Encoding (CARE) chip(Figure 6) [11] has therefore been adopted. The two preamplifiers on each crystal,A and B, each provide x1 and x32 gain outputs in order to reduce the dynamic range on the data transmission within the calorimeter from 18 bit to 13 bit. The CARE chip initially combines the two signals as an average of A and B, but also provides the option to read out A or B separately for diagnostics purposes. The signal is then further post-amplified to provide signals of gain 256,32,4 and 1 which are used for the energy ranges 0-50 MeV,50-400 MeV,0.4-3.2 GeV,3.2-13.0 GeV respectively. The signal is

identified in range with a comparator circuit and then input into a 10 bit, 4 Mhz ADC. Signals from 24 crystals are then multiplexed onto a fiber optic driver and sent serially at a rate of 1.5 Gbits/sec across a 30m fiber optic cable to the ROM [12]. In the ROM the continuously digitized data stream is input to a digital pipeline. A correction for pedestal offset and the gain calibration is first applied to each sample. The pipeline is then tapped to form a digital trigger line that is input to the trigger [13]. An accept is passed back to the digital pipeline and the data samples within a time window of $\pm 1\,\mu$s of the decision are used for the feature extraction algorithm.

In the first year of operation the calorimeter feature extraction is implemented as a parabolic fit to the signal peak to derive the energy and time of the signal. It is planned to implement digital filtering prior to fitting to reduce the noise. The frequency decomposition of an average pulse and the typical noise spectrum are measured for all channels and then used to derive a set of weights, maximizing the signal to noise ratio. These weights are then applied to individual pulses.

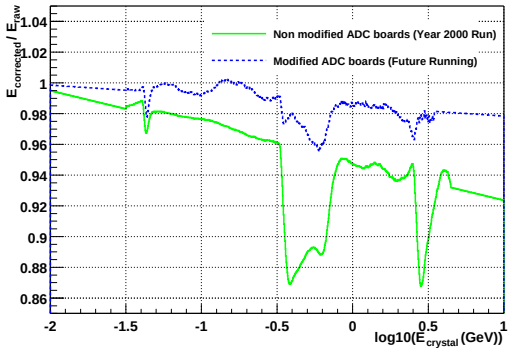

Figure 7. The deviation from linearity of the electromagnetic calorimeter observed during the first year of running. A perfectly linear calorimeter would have a constant value of 1.0 in this plot. The linearity for subsequent running following modifications to the electronics is also shown.

7.4.2. Electronics Calibration and Linearity

The electronics is calibrated to remove any pedestal offset and to correct for any non-linearities in the readout. The linearity calibration is performed using a charge injection circuit on the preamplifier.

Figure 7 shows the deviation from linearity observed in the detector during the first year of running. The non-linearity is caused by cross-talk as a result of design flaws in the digitization electronics. The effect will be reduced from the 12% effect shown to an irreducible 2% level for subsequent running. To ameliorate this problem we have developed a procedure to calibrate the linearity of the electronics using data. We accumulate a large amount of data and then study the energy spectrum of individual crystals. When compared to the expected distribution from Monte-Carlo simulations the non-linearities appear as a deviation from a smoothly falling spectrum. We therefore scale the spectrum using as anchor points the two single energy calibrations described in section 7.5.1 and require that it be smoothly falling. The efficacy of this procedure is confirmed by the substantial gains in resolution of electrons and photons.

7.4.3. Electronics Reliability

The calorimeter has been in operation for 1 year. With the exception of minor damage to preamplifier-ADB cables during final installation (leaving two channels inoperative), the system of 13160 readout channels has so far met its required reliability.

The reliability of the more accessible digitizing electronics was was initially very poor due to the Failure of a large number of optical fiber drivers. After replacement the reliability improved substantially leading to typical channel losses of less than 0.1% at any time.

7.4.4. Electronic Noise

The absolute contribution of electronic noise in the readout chain is measured as the rms of the pedestal. The measured spectrum of a 6.13 MeV photon source with two escape peaks is con-

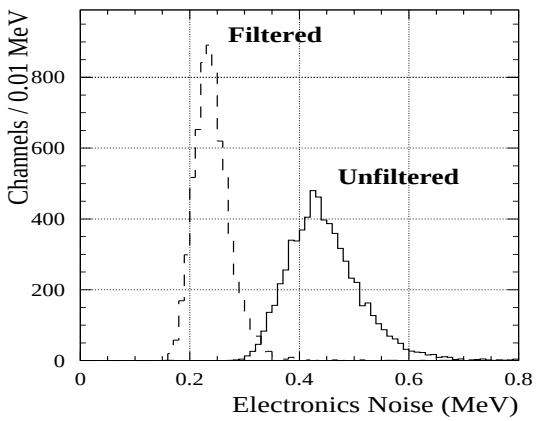

Figure 8. The distribution of equivalent noise energy for all channels of the Electromagnetic Calorimeter with/without digital filtering.

voluted with the electronic noise whose value is fitted for each crystal. Figure 8 shows the distribution electronic noise for all channels with and without digital filtering. The average electronic noise of 230(440) keV with (without) digital filtering is comparable to design expectations. Measurements of the autocorrelation function derived from digital filter weights from the source indicates that the grounding and shielding scheme adopted, has reduced the coherent noise component to a negligible level compared to the incoherent noise.

7.5. Calibration

The calibration relates the generated crystal scintillation light to the energy of the incident particle. An electromagnetic shower will typically span many adjacent crystals and a small fraction of energy will be lost by leakage from the rear of the crystal and in the material in front of, and between, the crystals. The calibration requires two steps. First the individual crystals are calibrated to the actual energy deposited. Second the energy sum of the "clusters" of adjacent crystals must be corrected for energy loss. The offline pattern recognition procedure that groups these crystals together in "clusters" is described in detail in section 7.8.

7.5.1. Individual Crystal Energy Calibration

An energy dependent calibration of each crystal is required because the light yield is generally non-uniform along its length, and changes with time as it is exposed while in operation to radiation. The impact of radiation is greatest in the front of the crystal and results in the formation of color centers which increase the attenuation of the transmitted scintillation light. The calibration must therefore be performed at different energies and frequently enough to keep up with the beam induced radiation damage. Concerns with radiation damage have also led to the development of a precise monitoring system using a light pulser to track very short term changes.

The calibration to deposited energies is performed at two energies at opposite ends of the dynamic range and then connected by a logarithmic extrapolation. A 6 MeV circulating radioactive source technique has been developed while at higher energies (3-9 GeV) the relation between production angle and energy for Bhabha events has been exploited [3].

A 6.13 MeV photon is produced promptly from the reaction $^{16}O^{*} \rightarrow^{16} O\gamma$ after irradiating a fluorocarbon fluid (polychlorotrifluoroethylene) with a low energy neutron generator at a rate of 4×10^{8} neutrons per second, to produce $^{16}\mathrm{N} + \alpha, ^{16}\mathrm{N} \rightarrow^{16} \mathrm{O}^{*} + \beta$. In addition to the primary 6.13 MeV line there are also two associated escape peaks located at 511 and 1022 MeV below. The neutron generator is located adjacent to the detector in a protective bunker. The activated fluid, with a half life of ^{16}N is 7 seconds, is pumped rapidly from the generator to a series of 0.5 mm thick aluminum manifolds mounted immediately in front of the calorimeter. The typical rate of photons is 40 Hz at the front face of the crystal. The energy of these photons is significantly higher than from any conventional and readily available source and allows a precise calibration. The short half life guards against con-

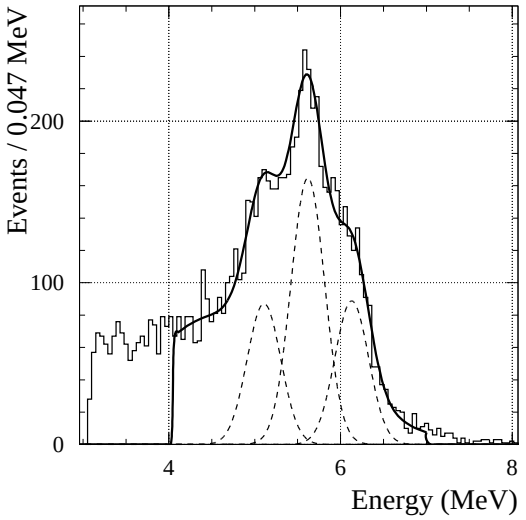

Figure 9. A typical pulse height spectrum for the radioactive source peak used to calibrate the single crystal energy scale of the Electromagnetic Calorimeter. The spectrum is a primary 6.13 MeV line with associated escape peaks 511 and 1022 MeV below.

cerns with contamination in the event of a fluid leakage. Even with the relatively high energy of the source it is necessary to implement a digital filter to extract the source peaks. The source is able to produce a calibration to a statistical precision of 0.35 % in a 30 minute run resulting in a systematic error of less than 0.1 %. Figure 9 shows a typical source spectrum. The calibration is performed weekly.

The high energy point of the single crystal calibration is performed with a pure sample of Bhabha events. The incident energy is known a-priori from the production angle with respect to the beam direction. The fraction of the shower energy in each crystal is estimated from a GEANT [5] based Monte-Carlo so that for each cluster the constraint may be written as a linear equation in the gain constant for each crystal. The accumulation of many events then results in a set of numerically soluble simultaneous linear equations. The frequency of calibration is set by the rate of degradation in response due to radiation damage. In the first year of running a calibration was performed every month. However the calibration has been automated so that we may increase the frequency as necessary. In a 12 hour running period at a luminosity of 3 $\times 10^{33}\mathrm{cm}^{-1}\mathrm{sec}^{-2}$ about 200 hits per crystal are accumulated, leading to calibration with statistical precision of 0.35 %. with a systematic error of yy.

7.5.2. Cluster Energy Correction

Following the single crystal calibration the cluster energies are corrected for energy loss from leakage and in the material in front of and between the crystals. The correction is a function of energy and polar angle $\cos\theta$. It is evaluated using π^0 candidates at low energy ($\mathrm{E} < 0.8\,\mathrm{GeV}$) [**?**]. The true energy of the particle may be expressed as the measured deposited energy multiplied by a correction function expressed as a polynomial in ln(E) and $\cos(\theta)$. The π^0 calibration constrains the two photon mass to the nominal π^0 mass and iteratively finds the coefficients of the correction function. The typical corrections are about $6 \pm 1\%$. The uncertainty in the correction is due to systematic uncertainties in the background estimation and the fitting technique.

At higher energy ($0.8\,\mathrm{GeV} < \mathrm{E} < 9\,\mathrm{GeV}$ we estimate the correction from simulated single photon Monte Carlo events. A data based technique using radiative Bhabha events has also been developed for future operation [4]. The beam energy and the precise tracking chamber measurements of the e^+ and e^- are used to fit for the radiative photon energy. This value is then used to extract the correction coefficients.

7.6. Monitoring

7.6.1. Environmental Monitoring

The temperature of the detector must be strictly controlled to prevent thermal stresses fracturing the photo-diode/crystal epoxy joint and also because the leakage current of the photo-

diode rises exponentially with temperature. The temperature is monitored by 256 thermal sensors placed throughout the detector and observed to be $22 \pm 0.5°C$ throughout the first year of operation. In addition the crystals must be kept in a dry environment as they are slightly hygroscopic. The dry nitrogen that circulates throughout the detector maintains a relative humidity of of $1 \pm 0.5\%$ at the operating temperature of 22°C.

7.6.2. Light Response

The light response of the individual crystals is monitored frequently (daily) using a light pulser system [6]. Light from a Xenon flash lamp transmitted through fiber optics to the rear of each crystal. The light pulse is similar in spectrum, rise time and shape to that produced from a CsI(Tl) scintillation. The pulses are varied in intensity by neutral density filters, allowing a precise measurement of the linearity of light collection, conversion to charge, amplification and digitization. The system is monitored pulse to pulse by comparison to a reference system utilizing two sources , ^{241}Am and ^{148}Gd, attached to a CsI(Tl) crystal readout by both a photo-diode and a photo-multiplier tube. The system is stable to 0.15% over a period of one week. The system has proved to be valuable in diagnosing problems during the commissioning of the detector. For example the ability to vary the light intensity facilitated the detection of non-linearities in the electronics.

7.7. Radiation Monitoring and Damage

The radiation dose received is monitored by a number of RadFETs placed in front of the crystals. A RadFET is a real-time integrating dosimeter based on solid state Metal Oxide SemiConductor (MOS) technology. There are 60/56 RadFETs in the endcap/barrel $3 \times 20/8 \times 7$ in $\theta \times \phi$. Figure 10 shows the integrated dose received in the endcap,forward barrel and backward barrel. The dose appears to follow the integrated beam currents, approximately linearly. The corresponding scintillation light losses due to radiation damage are shown. The loss is greatest in the forward region corresponding to the area of highest integrated radiation dose. The observed light loss fol-

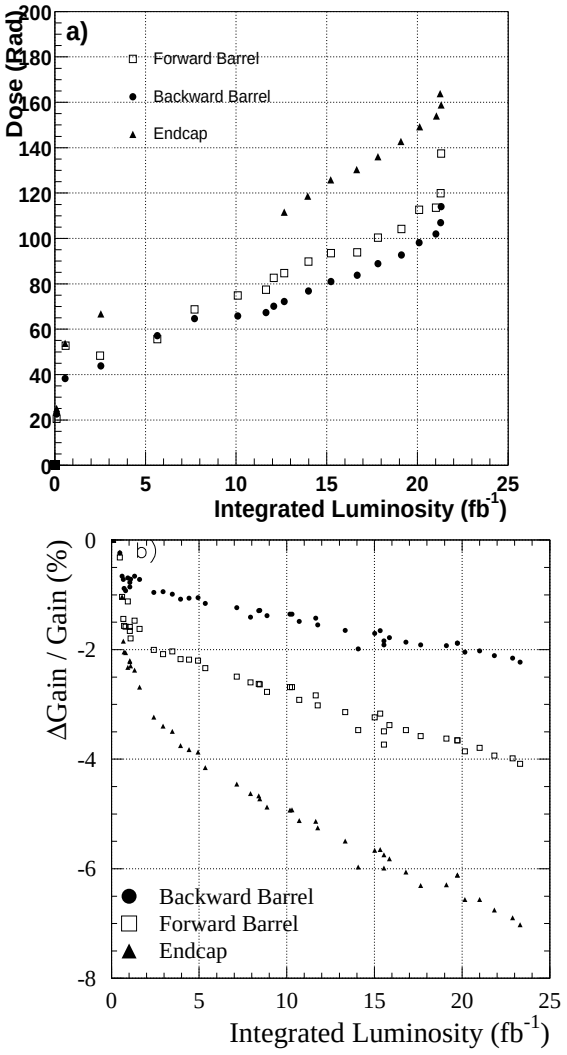

Figure 10. a) The integrated radiation dose received by the calorimeter measured using RadFETs place in front of the crystals. b) The degradation in light yield from the CsI(Tl) crystals measured with the radioactive source calibrator.

lows our expectations for the observed radiation dose.

7.8. Reconstruction Algorithms

A typical electromagnetic shower spans many adjacent crystals. The pattern recognition algorithms are required to efficiently identify these connected regions which we refer to as "clusters". Further they must be able to identify the most general case where several showers may be in close proximity and merge to form a single cluster with one or more local maxima referred to as "bumps". Lastly it must be determined whether the bump is associated with a charged or neutral particle by evaluating its proximity to a track.

Clusters are formed by demanding that an initial crystal contain at least 10 MeV. Neighboring crystals are included in the cluster if their energy exceeds 1 MeV. It is highly desirable to reduce this single crystal inclusion threshold as low as possible since fluctuations in the effective energy loss at the edges of a shower cause a degradation in resolution. In the first year of operation the threshold was set at 1 MeV to reduce the detector occupancy due to electronic noise. . If in addition the crystal energy is greater than 3 MeV, the crystal's contiguous neighbors (including corners) are considered for inclusion in the cluster. Local maxima crystals are located within a cluster by requiring the candidate crystal have an energy, $E_{LocalMax}$, which exceeds each of its neighbors and that satisfies a maxima condition [7]. Clusters are then divided into as many bumps as there are local maxima. Each crystal is given a weight, w_i

$$w_i = E_i \frac{\exp(-2.5 r_i/M_R)}{\Sigma_j E_j \exp(-2.5 r_j/M_R)}$$

where r_i is the 3-dimensional distance of the ith crystal from the centroid of the bump, and M_R is the Moliere radius. The denominator is a sum over all crystals in the cluster. At the outset, all weights are set to one. The process is then iterated, whereby the centroid position used in calculating r_i is taken using the weights from the previous iteration, until the bump centroid position is stable to within a tolerance of 1 mm . The energy of a cluster or bump is given by

$$E = \Sigma w_i E_i$$

In the case of a cluster with a single bump $w_i = 1$.

The position of the cluster is calculated by the logarithmic weighting method described in [8]. The simple center of gravity method tends to bias towards the center of the central crystals. The logarithmic method gives extra weight to smaller energy depositions further from the central crystal and removes this bias [9]. A further systematic bias derives from the non-projectivity of the crystals in the polar direction. This is corrected by a simple offset of -2.6 milliradians for $\cos\theta < 0$ and +2.6 milliradians for $\cos\theta > 0$.

Finally we determine whether the cluster/bump is associated with a charged or neutral particle by projecting a track to the inner face of the calorimeter. The track is corrected for energy loss under the pion hypothesis. A cluster is determined as neutral if the track does not intersect any of its crystals. To determine if a bump is neutral we compute the three dimensional distance from the track intersection point to the bump centroid. The distance is compared with the Monte Carlo expectation for different particle species with the measured track parameters.

7.9. Beam Backgrounds

In data taking, a single crystal energy threshold of 1 MeV is employed, below which the crystal energy is not read out. This threshold is limited by electronic noise, however there is also a significant contribution from low energy photons produced by beam-related backgrounds. These photons produce a characteristic pattern of energy deposition in the calorimeter which peaks in the forward and backward directions, and in the horizontal plane of the detector. Figure 11 shows the single crystal energy spectrum obtained using randomly triggered events while running with only a single beam in the machine. This flux of photons is reasonably well reproduced by Monte Carlo based lost-particle simulation of the accelerator and GEANT simulation of the detector. When the two beams are in collision, there is an additional flux of soft photons from zero-angle radiative Bhabha scattering in which the

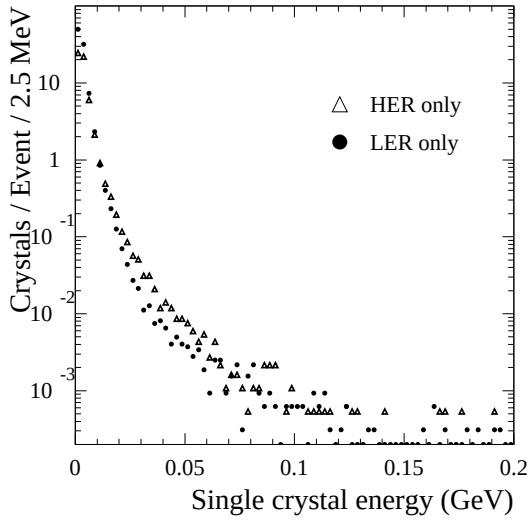

Figure 11. The energy spectrum of low energy beam related backgrounds observed in the Electromagnetic calorimeter. The events are taken using random triggers with only a single beam, either the high energy electron beam (HER) or the low energy positron beam (LER). The electronic noise spectrum has been subtracted.

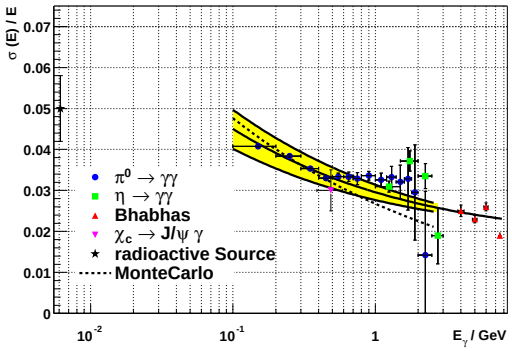

Figure 12. The energy resolution for the electromagnetic calorimeter measured using photon and electron candidates.

off-energy electron or positron strikes a machine element near the IP and initiates a shower. During typical running conditions, electronics noise combined with the background particle flux result in approximately 900 electronics channels being readout per event.

7.10. Performance

7.10.1. Energy Resolution

The energy resolution is measured directly with the radioactive source (Figure 9) at low energy and with electrons from Bhabha scattering at high energy (Figure 13) , yielding resolutions of $\sigma_{\rm E}/{\rm E} = 5.0 \pm 0.8\%$ at 6.13 MeV and $\sigma_{\rm E}/{\rm E} = 1.9 \pm 0.07\%$ at 7.5 GeV . Figure 12 shows the energy resolution extracted from a variety of data as a function of energy. The mass resolution of of π^0 and η candidates in which the two photons in the decay have approximately equal energy can be used to infer the energy resolution at an energy less than 1 GeV/c^2The resolution at higher energy is measured with electrons from Bhabha scattering and from the process $\chi_{c1} \rightarrow J/\psi\gamma$. The expectation from Monte Carlo is shown as the solid curve, where the contributions from electronic noise and low energy beam backgrounds are included. The data fits the curve given by equation 1 with $\sigma_1 = 2.32 \pm 0.30\%$ and $\sigma_2 = 1.85 \pm 0.12\%$. Figure 13 shows the measured energy/expected energy for Bhabha electrons. The width and shape of this distribution are consistent with Monte Carlo expectations.

7.10.2. Angular Resolution

Figure 14 shows the angular position resolution measured as a function of energy. The decays of π^0 and η candidates in which the two photons from the decay have approximately equal energy are used to infer the position resolution. It varies between about 12 milliradians at low energies and 3 milliradians at high energy. The expectation from Monte Carlo is shown in the solid curve.

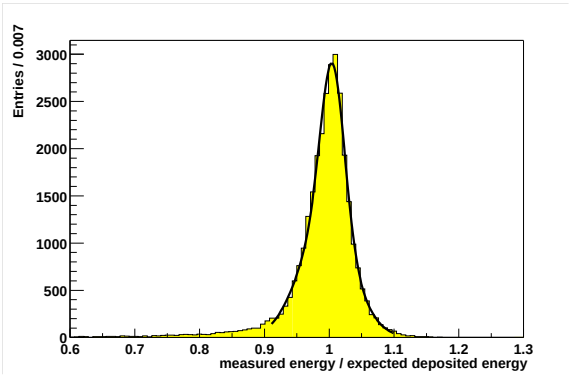

Figure 13. The measured energy/ expected energy for Bhabha electrons. The expected energy is known a-priori from the production angle.

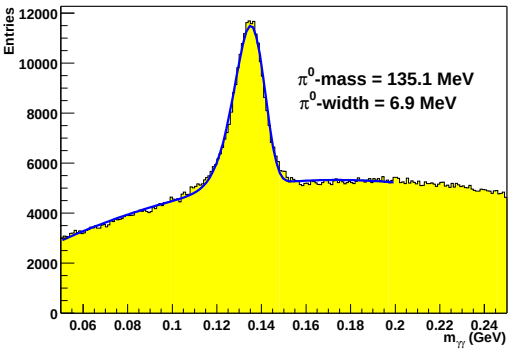

Figure 15. The π^0 mass peak reconstructed from photon candidates in hadronic events. The photon candidates are required to have an energy of at least 30 MeV and the energy of the π^0 must be greater than 300 MeV to reduce combinatoric backgrounds.

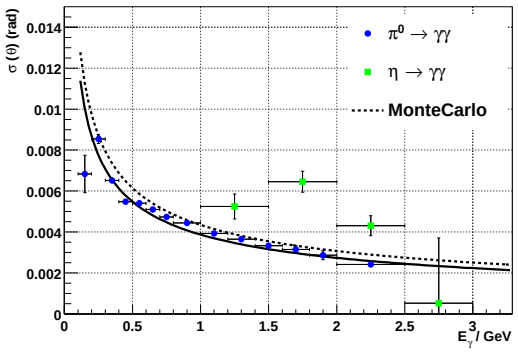

Figure 14. The position resolution for the electromagnetic calorimeter measured using photon and η candidates.

The data fit the empirical parameterization:

$$\frac{\sigma_{\theta,\phi}}{E} = \frac{\sigma_1}{\sqrt{E}} + \sigma_2 \qquad (2)$$

where $\sigma_1 = 3.87 \pm 0.07$ mr and $\sigma_2 = 0.00 \pm 0.04$ mr. The data is in good agreement with the Monte Carlo expectation.

7.10.3. π^0 Mass and Width

Figure 15 shows the two photon invariant mass for π^0 candidates. The π^0 candidates are taken from hadronic B-meson events. The invariant mass is stable to less than 1 % over the full photon energy range. The width of 6.9 MeV/c^2 compares to a Monte-Carlo estimate of 6.8 MeV/c^2 in hadronic B meson events. In low occupancy $\tau^+\tau^-$ events the width is observed to be 6.5 MeV/c^2 for π^0 energies below about 1 GeV/cİmproved resolution is also observed in hadronic events where only isolated photons are considered.

7.10.4. Electron-Hadron Separation

Electron hadron separation is accomplished by use of the shower energy, lateral shower moments

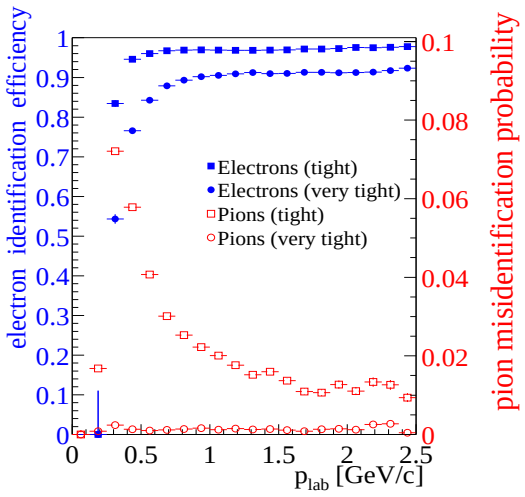

Figure 16. The electron efficiency and pion misidentification rate for different momenta.

and incident track parameters. The comparison of shower energy and incident momentum (E/p) is the most significant separation variable. Figure 16 shows the electron efficiency and pion misidentification rate for different momenta using a cut based selection algorithm. The efficiency of electron identification is measured using electrons from radiative Bhabhas and $\gamma\gamma \to e^+e^-$ events. The pion misidentification probability is measured three prong τ decays. The *tight* selector has an average efficiency of 94.8 % in the momentum range $0.5\,\mathrm{GeV}/c < p < 2\,\mathrm{GeV}/c$, with a pion misidentification probability of roughly 1.2 %. The *very tight* selector has an efficiency of 88.1 % with an average pion misidentification of 0.3 %. The electron-hadron separation power meets design expectations.

7.11. Conclusion and future

In conclusion the calorimeter has been designed, constructed, and installed. It has been demonstrated to be a reliable and stable detector in one year of operation. It is presently performing close to design expectations. We expect substantial improvement in the energy resolution in the near future by optimizing the feature extraction algorithms to reduce the effect of electronic noise. These improvements should in addition allow the reduction of the single crystal energy threshold for inclusion into the cluster. The repair of design flaws in the electronics hardware should also allow a more precise calibration.

REFERENCES

1. "The BaBar Technical Design Report" D. Boutigny *et al.* SLAC-R-457
2. The CsI salt was purchased from Chemitall and APL. The crystals were grown, machined and polished by Shanghai Institute of Ceramics, China Beijing Glass Research Institute, China Hilger Analytical, United Kingdom Crismatec , France Amcrys-H, Ukraine.
3. R. Mueller-Pfferfercorn "Die Kalibration des elektromagnetischen CsI(Tl)-Kalorimeters des Babar-Detektors mit Ereignissen der Bhabha-Streuung" Ph.D Thesis, Techical University of Dresden, Germany, 2000 TUD-IKTP/01-01
4. J. Bauer "Radiative Bhabha Calibration for the BaBar Electromagnetic Calorimeter ", SLAC-PUB 8650, 2000.
5. "GEANT Detector Description and Simulation tool " CERN Program Library Long Writeup W5013, 1994.
6. M. Kocian "Das Lichtpulsersystem des elektromagnetischen CsI(Tl)-Kalorimeters des Babar-Detektors" Ph.D Thesis, Techical University of Dresden, Germany, 2000 TUD-IKTP/00-03
7. $0.5(N-2.5) > \dfrac{E_{NMax}}{E_{LocalMax}}$ where E_{NMax} is the highest energy neighbor of the crystal and N is the number of neighbors of the crystal whose energy exceeds

2MeV.

8. B.Brabson et al, Nucl. Inst. and Methods, A332 (419-443) 1993. eqn 14.
9. The logarithmic weight,$\mathrm{lw_{crystal}}$ used to compute the centroid of the cluster is

$$\mathrm{lw_{crystal}} = 4.0 + \ln \frac{\mathrm{E_{crystal}}}{\mathrm{E_{cluster}}}$$

10. We use model S-2744-08 PIN diodes manufactured by Hamamatsu Photonics, K. K. , Japan. The dark current is specified to be less than 5nA and the capacitance to be less than 105 pf at the nominal depletion voltage of 70V. In 13500 diodes we observed a typical dark current of 4 nA and capacitance of 85pf.
11. G. Haller and D Freytag IEEE Trans.Nucl.Sci.43:1610-1614,1996
12. The BaBar Data Acquisition.
13. The BaBar Trigger.